Modeling cohesive granular flows: Kinematics, rheology, and morphology

Fanshuo Ma, Stéphanie Deboeuf, Pierre-Yves Lagrée, and Lydie Staron
Sorbonne University, CNRS, Institut Jean le Rond d'Alembert, F-75005 Paris, France

(Received 20 March 2025; accepted 22 May 2026; published 22 June 2026)

A model for stationary cohesive granular flows on inclines is proposed based on the assumption of an ideal Coulomb material supplemented with a linear $\mu(I)$ dependence. For assessing the reliability of the model, discrete numerical simulations are carried out in two dimensions, varying both contact adhesion and flow slope on a large range of values. Focusing both on the surface velocity and on the thickness of the surface plug flow, a systematic comparison between discrete simulations data and analytical predictions derived from the model allows for testing the latter. In particular, the ideal Coulomb material hypothesis, including the independence of friction and cohesion, is corroborated, together with the applicability of the linear approximation of the $\mu(I)$ flow law. Confronting model and discrete simulations discloses a linear relation between macroscopic cohesion stress and local contact adhesion, in agreement with Rumpf's prediction. The bottom velocity is shown to obey a Navier-Robin condition with a slipping length poorly dependent on adhesion properties. In addition, the analysis of the surface topography shows how increasing contact adhesion leads to a more craggy surface line. In the context of a simplified flow configuration, the present work brings clarification on the intricate roles of contact adhesion and flow dynamics on the cohesive behavior of granular flows. It allows for testing the relatively simple theoretical framework and hypothesis used to derive analytical solutions, thus showing that many salient features of cohesive flows are captured by basic ingredients. Based on relatively accessible quantities in laboratory measurements, it may also shed an interesting light on experimental work.

DOI: 10.1103/w1xz-9dbv

I. INTRODUCTION

Dense gravity-driven granular flows are highly relevant to industrial applications (agricultural transportation, pharmaceutical industries, etc.) and natural phenomena (rock avalanches, landslides, etc.) [1]. While better understanding has been achieved in the noncohesive case, where grain interactions are dominated by friction and viscoelastic contact forces, the existence of adhesive contact forces significantly modifies the behavior of systems [2,3]. This may affect our understanding of natural phenomena, for instance, the catastrophic flow of wet debris or rock material often studied applying the column collapse configuration [4,5]. It is also an issue in engineering practice, for instance, mixing in rotating devices [6].

In the simpler case of chute flows along channels, contact adhesion affects the velocity profile, hindering motion and inducing clogging, and possibly changing the aspect of flow surfaces or deposits. These aspects have prompted a large number of studies, without a definite picture of cohesive granular matter being reached. In terms of flow kinematics, the well-known Bagnold velocity profile characterizing dry flows [7,8] no longer holds in the presence of adhesive contacts, and a plug region appears at the surface [9–12]. Recently, Vo *et al.* have augmented the widely used $\mu(I)$ rheology to include cohesive effects [8,13]; applied to the modeling of cohesive flows, this extended inertial number allows for recovering the plug thickness, thus providing a promising step forward [14].

Another macroscopic aspect pertaining to the existence of adhesive contacts is the formation of grain agglomerates in cohesive flows. Specific surface patterns may appear on the surface as a consequence [11,15,16]. Tapia *et al.* studied the morphology of fractures of granular systems held in a humid atmosphere causing contact adhesion by capillarity, and showed the existence of a characteristic length of fracture roughness depending on the air humidity [17]. By means of discrete numerical method, Abramian *et al.* studied the deposit left by a granular collapse and related the deposit surface roughness to contact adhesion strength [16]. Preud'homme *et al.* likewise related flow surface fluctuations and contact adhesion [11]. More recently, Deboeuf and Fall conducted experimental studies of cohesive granular flows over an inclined plane, and achieved a better agreement between data and theory by introducing a cohesive aggregate size [12].

In effect, the way cohesive strength relates to the local contact adhesive force is not a resolved issue. In his pioneering work, Rumpf related the tensile strength of an assembly of particles to the mean contact adhesive force, packing friction and steric properties [18]. Various authors have compared their results to this seminal work, recovering the predicted dependence, yet without allowing new insight in the adhesion-to-cohesion mechanism [19–21].

Finally, wall slip in noncohesive granular flows is reported in different flow configurations, and its advent in cohesive conditions is worth assessment [22–24].

All these aspects, namely, the emergence of a macroscopic effective cohesion and its effect on flow behavior, its dependence on local contact adhesion and packing characteristics, and its signature in the shape of agglomerates occurrence, are questions of interest [25]. In this contribution, we develop an analytical solution for cohesive granular flows on inclines, and compare it with two-dimensional discrete simulations allowing to explore different adhesion strength and flow slopes. Quantities such as plug height and velocity profile, extracted from discrete simulations, allow for relating the macroscopic cohesive stress τ_c to the contact adhesion intensity, thus questioning the Rumpf prediction. Meanwhile, the consistency between simulation and predictions give a means to assess the relevance of the cohesive rheology underlying the model, namely, the ideal Coulomb material assumption supplemented with a linear dependence of friction to flow inertia. The independence of cohesive stress and frictional properties is questioned and confirmed, and so is the independence of cohesive properties on inertia. Meanwhile, the study of the surface roughness shows how the latter increases with adhesion strength, in agreement with earlier work [16,17]. The analysis of bottom velocity reveals a slip condition consistent with a Robin-Navier condition, with a slipping length essentially independent of adhesion strength but for large velocities.

The results endorse the use of the relatively simple theoretical framework and hypothesis used to derive analytical solutions, thus showing that many salient features of cohesive flows are captured by basic ingredients. It also provides interesting observations of a phenomenology which is not necessarily easy to capture experimentally, keeping in mind the simplification resulting from the two-dimensional (2D) configuration.

The work is organized as follows. The discrete numerical method and simulation setup are introduced in Sec. II. In Sec. III, a theoretical continuum model for a 2D steady uniform flow over an inclined plane is proposed, based on an ideal Coulomb assumption supplemented with a $\mu(I)$ dependence. In Sec. IV, the flow morphology involving a surface plug region and surface roughness is studied. Section V confronts the predictions of the model with the outcome of the discrete simulations. The results are discussed and summarized in Sec. VI.

II. NUMERICAL PROCEDURE

A. Method

A contact dynamics (CD) algorithm is used in two dimensions to simulate the flow of granular beds on inclined planes. Unlike explicit numerical methods such as molecular dynamics (MD) or

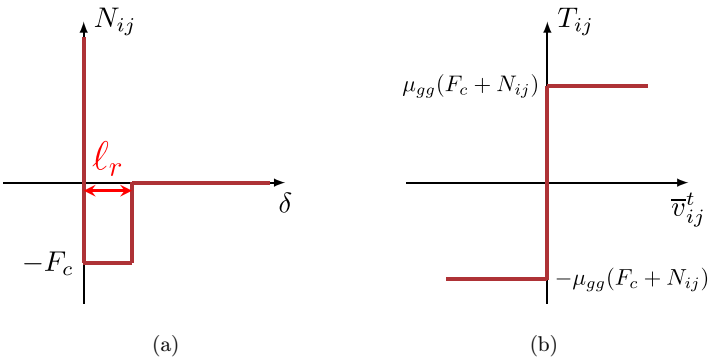

FIG. 1. Contact graphs for normal contact force N_{ij} and tangential contact force T_{ij}, with the red line showing the admissible values for the force: (a) Signorini law supplemented with an adhesive contact limit $-F_c$ and a rupture length ℓ_r; (b) Coulomb friction law with intergrain friction coefficient μ_{gg}.

the discrete element method (DEM) [26], contact forces are computed implicitly from dynamics equations and nonsmooth Signorini-Coulomb contact laws, as illustrated in Fig. 1 [27]. The former essentially ensures the noninterpenetrability condition, or, in other words, the rigidity of the grains. Readers can refer to Ref. [28] for a comprehensive presentation of CD.

Interactions at contact are also controlled by Coulomb friction, set by the contact friction coefficient μ_{gg}, and by elastic restitution, set by normal and tangential restitution coefficients, e_n and e_t, respectively [28]. Their values remain the same throughout the present work, namely, $\mu_{gg} = 0.2$ and $e_n = e_t = e = 0$. By setting the restitution coefficients to zero, we assume inelastic collisions at contacts, which is reasonable for adhesive interactions. It is, however, worth noting that the value of the restitution coefficient, in the limit of moderate values, has little influence on flow properties, because dissipation through multiple collisions is very efficient. This aspect is specifically addressed in the Appendix.

Figure 1 shows the values of contact normal forces admissible in the adhesive hysteretic version of Signorini's graph used in this work. The graph is shifted toward negative values, to allow for tensile stress at contact between two grains. This tensile (adhesive) force is characterized by a threshold, giving the maximum adhesive force sustainable at contact. We choose to express this adhesive force threshold F_c as a function of the grains' mean weight, introducing the granular Bond number Bo_g [10] :

$$F_c = \mathrm{Bo}_g m_{ij} g, \tag{1}$$

where $m_{ij} = 2(\frac{1}{m_i} + \frac{1}{m_j})^{-1}$, and i and j are the two grains in contact. The system's cohesive level can thus be varied by tuning the grains' normalized adhesive force strength $\mathrm{Bo}_g = F_c/mg$ [29,30].

Moreover, Fig. 1 represents how the tensile force can outlive a finite opening of the contact (i.e., $\delta > 0$). This effect mimics the existence of capillary bridges in unsaturated wet media, involving a hysteresic behavior: adhesive contacts will survive when the contact is opening up to ℓ_r, but no adhesive contact forms while two grains approach until they are actually physically in contact. In practice, the algorithm does not use explicitly this part of the graph to solve contact forces, the graph branch being shown simply to convey the correspondence between forces and distance at contact. Numerically, the survival of the adhesive force at an opening contact is achieved by introducing locally a rupture (or debonding) length, which causes existing tensile contact to be further detected when grains move apart. Therefore, we define the rupture length $\ell_\mathrm{r} = k_\mathrm{r} d$, d being the mean radius of the contacting grains: a cohesive contact will not vanish until the gap between the two grains in contact has increased beyond ℓ_r. However, in this work, we do not aim at mimicking wet granular matter, for which $k_\mathrm{r} \approx 1 \times 10^{-1}$. Instead, we choose $k_\mathrm{r} = 5 \times 10^{-4}$, which would rather correspond

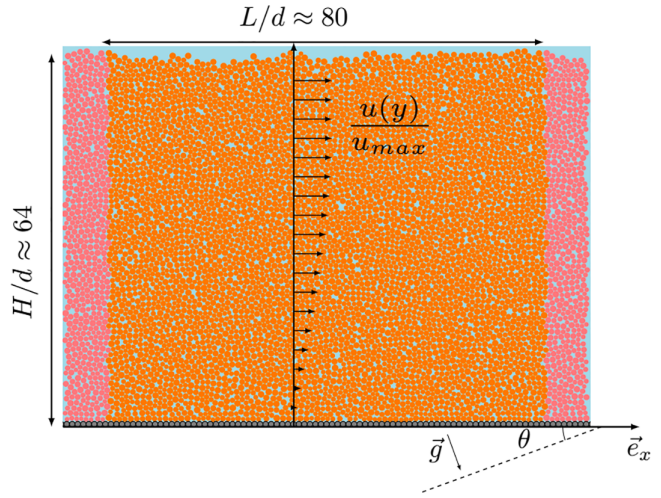

FIG. 2. Example of a 2D granular system counting 5280 grains with length $L \approx 80d$ and height $H \approx 64d$. Orange indicates free-moving particles, pink indicates grains images through periodic boundary conditions, and dark gray indicates grains glued at the bottom. The angle θ gives the orientation with the horizontal defined by gravity.

to a polymeric coating such as designed by Gans *et al.* [31]. Although very small, the existence of this rupture length has a stabilizing effect on the computation of contact forces [29]. The value of ℓ_r is kept constant in this work.

B. Numerical setup

We simulate 2D granular free surface flows over an inclined plane with periodic conditions in the longitudinal direction. The system is created by allowing 5280 grains initially distributed on a regular hexagonal mesh to fall under a reduced gravitational acceleration to limit initial grain overlap. Grain diameters are uniformly distributed in $[d_{\min}, d_{\max}]$ with $d_{\max}/d_{\min} = 1.5$ and mean grain diameter $d \approx 5 \times 10^{-3}$ m. The bottom is made rough with grains with the same diameter d; the contacts involving free-flowing grains only, or involving a bottom roughness grain, have the same properties. The final state forms a packing of length $L \approx 80d$ and height $H \approx 64d$ (Fig. 2).

The system is then tilted at an angle θ with the horizontal to produce a flow under gravity $g = 9.8\ \mathrm{m\,s^{-2}}$. Each simulation is allowed to run 5×10^5 time steps with $\Delta t = 2 \times 10^{-4}$ s, which corresponds to approximately $555\sqrt{H/g}$ and allows for a stationary regime to fully develop over the last $300\sqrt{H/g}$. Simulation outcomes (grain positions, velocities, and contact forces) are recorded at each $500\Delta t$, meaning approximately every $0.5\sqrt{H/g}$. The present study focuses on the stationary flow regime.

C. Typical behavior

To capture the phase diagram of the flows thus simulated, we vary the inclination angle θ in the range $[12^\circ : 28^\circ]$, while the contact adhesion Bo_g is varied in the range $[0 : 50]$, thus carrying out 69 simulations. The system height is fixed: $H \approx 64d$.

The outcome is shown in Fig. 3(a). For small inclination angles, no flow starts beside slight grain rearrangements at the surface: we refer to this phase as the "no-flow regime." For large inclination angle, the flow keeps accelerating: we refer to this phase as the "accelerated flow regime." Between these two regimes, the system reaches a steady uniform state, characterized by a constant velocity. This picture holds for the whole range of values explored. However, larger values of Bo_g increase

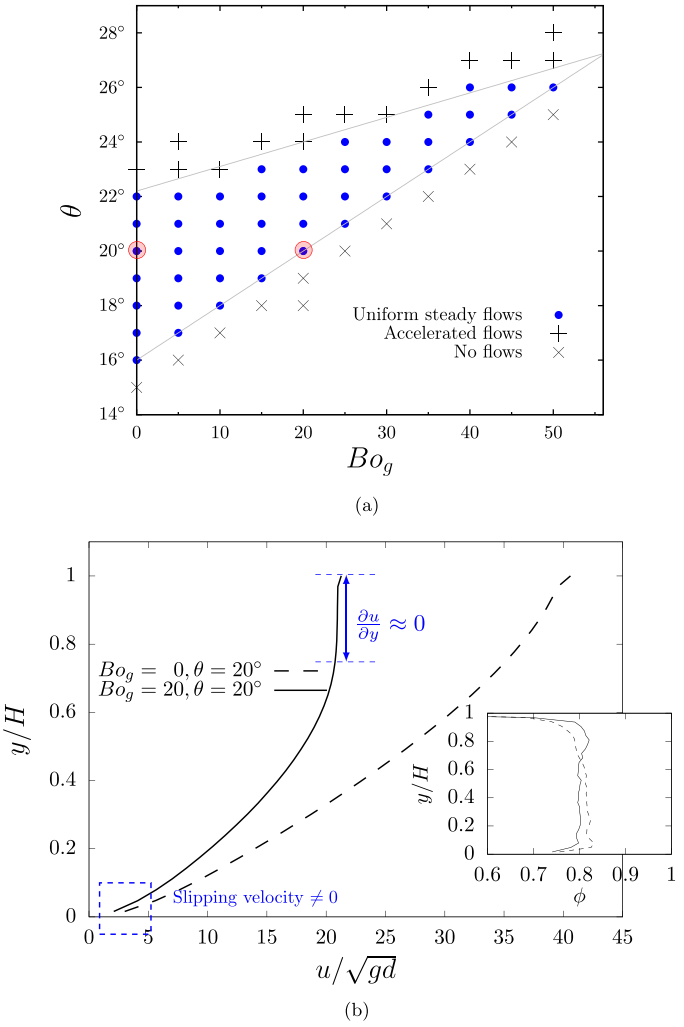

FIG. 3. (a) Flow phase diagram: existence of a steady uniform flow over an inclined plane, in the range of parameters $\theta \in [16^\circ : 26^\circ]$, $\mathrm{Bo}_g \in [0 : 50]$. (b) Velocity profiles corresponding to the two circled points, with respectively $\mathrm{Bo}_g = 20$ (solid line) and $\mathrm{Bo}_g = 0$ (dashed line). Inset graph shows the corresponding volume fraction profiles with the same line-style convention.

the inclination for which flow starts, and reduce the interval of angle θ in which a steady uniform flow is observed. Eventually, beyond $\mathrm{Bo}_g = 50$, the whole granular layer forms a cohesive plug, and no flow is observed any longer, independently of the value of θ.

Our results are consistent with previous studies [32,33], although direct comparison is made difficult by the flow conditions (two versus three dimensions, numerical versus experimental) or the differences in numerical parameters (different grain properties).

For illustration, Fig. 3(b) shows the mean velocity profiles in the steady flow regime, for adhesive grains ($\mathrm{Bo}_g = 20$) and nonadhesive grains ($\mathrm{Bo}_g = 0$), flowing on a plane inclined at $\theta = 20^\circ$. We observe how cohesion induces a slower motion and the emergence of a zero-shear region (plug) at the surface, the thickness of which is denoted H_c in the following. The volume fraction ϕ is also displayed in Fig. 3(b), exhibiting a nearly constant profile of $\phi \approx 0.8$, which makes the hypothesis of flow incompressibility reasonable. In both cases, the bottom slipping velocity is nonzero.

III. A THEORETICAL MODEL

In this section we derive the velocity profile of a 2D steady incompressible uniform flow on an incline satisfying a linearized $\mu(I)$ dependence [34]. The flow consists of a layer of constant thickness H, inclined at an angle θ with the horizontal, and uniform in the longitudinal (x) direction. The equilibrium equations between the pressure $P(y)$ and the tangential stress $\tau(y)$ give

$$\begin{aligned} P(y) &= \phi\rho g(H-y)\cos\theta, \\ \tau(y) &= \phi\rho g(H-y)\sin\theta, \end{aligned} \tag{2}$$

with $\tan\theta = \tau(y)/P(y)$.

Following Refs. [16,21], we suppose stresses to combine a Coulomb contribution, given by the effective friction coefficient μ of the media and the pressure P, and a cohesive stress τ_c:

$$\tau = \mu P + \tau_c, \tag{3}$$

assuming that friction μ and cohesion τ_c are independent properties [19,35].

In addition, we suppose a dependence between the friction coefficient μ and the inertial number I,

$$I = \frac{d\dot{\gamma}}{\sqrt{P/\rho}}, \tag{4}$$

where $\dot{\gamma} = \partial u(y)/\partial y$ is the local shear rate [8]. The nature of the dependence between friction and inertia is not a settled point [36,37]. However, for simplicity, we slightly deviate from the "classical" form adopted in Refs. [38,39] and propose a linearized version of the latter:

$$\mu(I) = \mu_0 + \frac{\Delta\mu}{I_0} I, \tag{5}$$

which is reasonable for relatively small values of $I \lesssim 0.3$. The term μ_0 designates the static friction coefficient, and $\Delta\mu/I_0$ renders both the final value of friction for larger I through the term $\Delta\mu$, and the shape of the evolution through the term I_0. The values of μ_0 and $\Delta\mu/I_0$ are both material dependent. Since it is assumed that friction and cohesion are independent properties, μ_0 and $\Delta\mu/I_0$ are independent of the contact adhesion Bo_g. Both quantities can thus be calibrated from discrete simulations with $\mathrm{Bo}_g = 0$, which is done later in Sec. V A. Likewise, the independence of cohesive stress τ_c on friction requires that τ_c is independent of I. The validity of both assumptions is verified in Sec. VI.

Combining equilibrium equations (2) and rheology equations (3) and (5), we get

$$\tan\theta = \mu(I) + \tau_c/P = \mu_0 + \frac{\Delta\mu}{I_0}\frac{d\dot{\gamma}}{\sqrt{P/\rho}} + \frac{\tau_c}{P}, \tag{6}$$

which can be rewritten

$$\dot{\gamma}\sqrt{\frac{H}{g}} = \frac{\partial u}{\partial y}\sqrt{\frac{H}{g}} = K_1\left(1-\frac{y}{H}\right)^{1/2} - K_2\left(1-\frac{y}{H}\right)^{-1/2}, \tag{7}$$

where K_1 and K_2 are dimensionless parameters:

$$\begin{aligned} K_1 &= (\tan\theta - \mu_0)\frac{I_0}{\Delta\mu}\sqrt{\phi\cos\theta}\frac{H}{d}, \\ K_2 &= \frac{I_0}{\Delta\mu}\frac{1}{\sqrt{\phi\cos\theta}}\frac{\tau_c}{\rho g d}. \end{aligned} \tag{8}$$

For noncohesive flow, $\tau_c = 0$ and hence $K_2 = 0$: the shear rate is zero only at the flow surface, for $y = H$. For a cohesive flow, for which the surface is characterized by the existence of a plug of

thickness H_c, the shear rate is zero throughout the plug, from the free surface $y = H$ to the bottom of the plug at $y = H - H_c$. Equation (7) thus gives

$$\frac{H_c}{H} = \frac{K_2}{K_1},$$

which leads to

$$\frac{H_c}{H} = \frac{1}{(\tan\theta - \mu_0)\phi\cos\theta}\frac{\tau_c}{\rho g H}. \tag{9}$$

Accordingly, the knowledge of H_c for a given flow may inform us on the value of τ_c. We note that the plug thickness H_c is controlled both by the cohesive stress τ_c and the tilt angle θ.

Finally, integration of Eq. (7) between zero and $y = H - H_c$ gives

$$\frac{u(y)}{\sqrt{gH}} = \frac{2}{3}K_1\left[1 - \left(1 - \frac{y}{H}\right)^{3/2}\right] - 2K_2\left[1 - \left(1 - \frac{y}{H}\right)^{1/2}\right] + \frac{u_{\text{slip}}}{\sqrt{gH}}, \tag{10}$$

where u_{slip} is the bottom slip velocity.

We denote $u_{\max}$ the maximum velocity, reached at the bottom of the plug flow for $y = H - H_c$. From Eqs. (9) and (10), we obtain

$$\frac{u_{\max}}{\sqrt{gH}} = \frac{2}{3}K_1 - 2K_2 + \frac{4}{3}K_1^{-1/2}K_2^{3/2} + \frac{u_{\text{slip}}}{\sqrt{gH}}. \tag{11}$$

Both H_c and $u_{\max}$ are functions of τ_c. It is, however, interesting to note that while both are dependant on the static friction μ_0, only $u_{\max}$ is reflecting the frictional properties developed during the flowing phase through the term $\Delta\mu$.

A no-slip condition implies $u_{\text{slip}} = 0$. However, research on noncohesive flows generally reports the existence of nonzero slip velocities with system boundaries, and, more specifically, a behavior consistent with the Robin-Navier condition (also known as a "mixed boundary condition") was evidenced [22,23]. We may suppose these observations to remain relevant for cohesive flows (questioned in Sec. V E). Accordingly, we assume

$$u_{\text{slip}} = \lambda_{\text{slip}}\left.\frac{\partial u}{\partial y}\right|_0, \tag{12}$$

where λ_{slip} is the slipping length. Expression (7) for $y = 0$ gives readily

$$\frac{u_{\text{slip}}}{\sqrt{gH}} = (K_1 - K_2)\frac{\lambda_{\text{slip}}}{H}. \tag{13}$$

The model gives a complete description of the kinematics of 2D steady cohesive flows, providing a few hypotheses, all verified in the course of the paper. In Sec. V, discrete CD simulations of cohesionless flows are used to calibrate the rheology given in Eq. (5). The systematic comparison of analytical solutions and discrete simulations of cohesive flows gives a means to relate the macroscopic cohesive stress τ_c to the microscopic contact adhesion force F_c, allowing comparison with existing prediction [18], as will be discussed in Sec. V D.

IV. MORPHOLOGY

The general morphology of the flow, i.e., the crust or plug flow forming in the upper part of the layer, or the roughness changing the aspect of the free surface, is known to be dependent on the flow cohesive properties [16,17]. In this section, we characterize the flow morphology, and relate it to the intensity of the contact adhesive force. The study of the plug region, in addition, gives a means to test the analytical model developed in Sec. III, while comparing the discrete simulation and the continuum picture (Sec. V C).

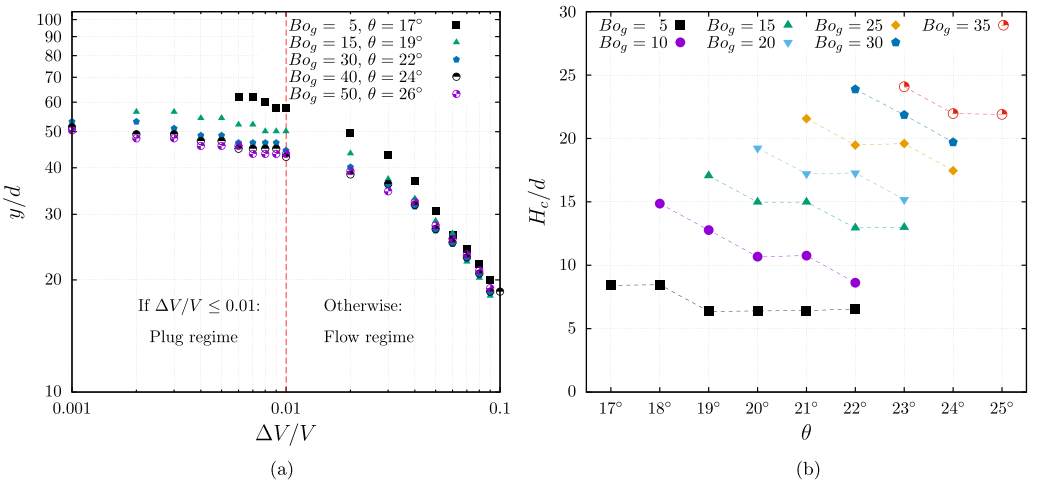

FIG. 4. (a) Relative velocity variation $\Delta V/V$ as a function of the position in the flow, y, for different slope angle θ and contact adhesion intensity Bo_g. (b) Plug region thickness H_c as a function of the tilt angle θ, for all values of contact adhesion Bo_g.

A. Plug region

The emergence of a surface plug region is a robust feature of cohesive flows [9,10,20,40]. The flow mean velocity profile gives a means to measure plug thickness H_c, provided a nonambiguous measurement of the position y where shear vanishes is achieved. From the shape of velocity profiles as shown in Fig. 3(b), we observe that the exact position where $\dot{\gamma}$ becomes zero is not clearly defined. Close inspection shows that flow moves with a weak creeping velocity difference between layers, which makes the identification of a plug region ambiguous. Therefore, to probe the existence of a cutoff value in the shear profile, we focus on the relative variations of velocity with height, dividing the flow in horizontal layers of thickness d, and comparing with the mean velocity at the considered height.

Considering two adjacent layers at $y = l$ and $y = l + 1$, we compute

$$\left(\frac{\Delta V}{V}\right)_l = \frac{V_{l+1} - V_l}{V_l}, \tag{14}$$

where $V(l)$ refers to the mean velocity computed from the grains located in layer l. Figure 4(a) shows the profile of $(\frac{\Delta V}{V})$ for different flows corresponding to different incline slope θ and different cohesion Bo_g. We first observe that all flows tend to exhibit the same tendency, but for weakly cohesive ones ($\mathrm{Bo}_g = 5$ and $\mathrm{Bo}_g = 15$), $\Delta V/V$ shows no major changes until it exceeds the value 0.01. We define Y_c as the value of the height y when $\Delta V/V$ reaches 0.01, which gives us the thickness of the plug, $H_c = H - Y_c$ (H being the height of the flow).

From Fig. 4(a), the choice of a cutoff value $\Delta V/V = 0.01$ is not entirely indisputable, yet we chose this value to determine the value of Y_c for all flows featured in Fig. 3. The sensitivity of the results to the value of the cutoff will be discussed in Sec. V A.

The results are displayed in Fig. 4(b), showing the thickness of the plug, H_c/H, as a function of the slope angle θ, for all the values of the contact adhesion Bo_g explored. The discrete simulation points show how larger adhesion induces a thicker plug, consistently with the literature [9,10], and how larger slopes, and hence larger velocities, tend to induce a thinning of the former. This measure of H_c will be used in Sec. V to discuss the model developed in Sec. III and the dependence linking macroscopic friction τ_c and contact adhesion Bo_g.

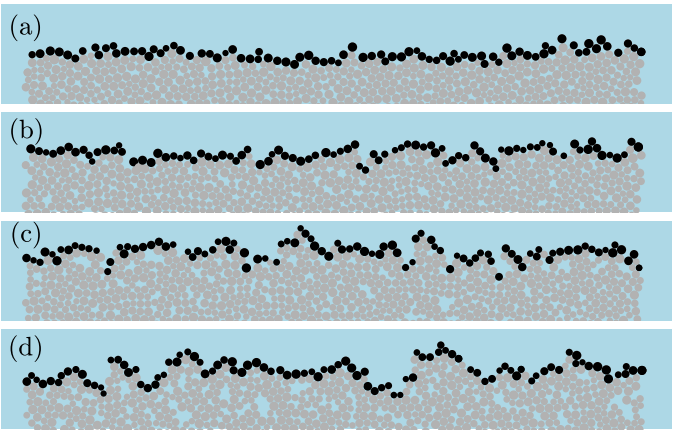

FIG. 5. Snapshots of the flow upper layers with grains on the surface colored in black: (a) $\mathrm{Bo}_g = 0$, $\theta = 16^\circ$; (b) $\mathrm{Bo}_g = 15$, $\theta = 20^\circ$; (c) $\mathrm{Bo}_g = 30$, $\theta = 24^\circ$; (d) $\mathrm{Bo}_g = 50$, $\theta = 26^\circ$.

B. Surface roughness fluctuations and spatial correlation

For cohesive granular flows for which surface grain motion and deformation are hindered, surface roughness is expected to result from the formation of aggregate due to the adhesive forces, and thus is dependent on adhesion intensity [12,16]. To investigate this aspect, we characterize the surface roughness through the fluctuations of the surface profile regarding its mean level.

Figure 5 shows four snapshots of the flow surface with different tilt angle θ and adhesive contact strength Bo_g. The surface grains are colored black. We notice that the surface becomes more jagged as Bo_g and θ increase, defining a growing roughness. To characterize this surface roughness, we compute the mean free surface height $\bar{h}(t)$ at each time step, and measure the fluctuations of the surface profile $h(x,t)$ compared to $\bar{h}(t)$:

$$\eta(x,t) = h(x,t) - \bar{h}(t). \tag{15}$$

In the following, we neglect the existence of correlations in time, and focus on the distribution of values of $\eta(x,t)$ recorded over the whole duration of the stationary flow regime considered. The probability density function (PDF) for the four examples featured in Fig. 5 (namely, for $\mathrm{Bo}_g =$ 0, 15, 30, and 50, and $\theta = 16^\circ$, 20°, 24°, and 26°) are displayed in Fig. 6(a). We observed bell-shaped distributions compatible with Gaussian functions $f(x) = \frac{1}{\sigma\sqrt{2\pi}} \exp(-\frac{(\eta-\bar{\eta})^2}{2\sigma^2})$, with standard deviations σ taking different values for each (Bo_g, θ) pair. Larger standard deviations coincide with broader distributions, i.e., larger values of η bespeaking larger roughness. The plot of σ as a function of θ for all pairs (Bo_g, θ) is displayed in Fig. 6(b). Except for the noncohesive case $\mathrm{Bo}_g = 0$, we see that the influence of the slope θ is marginal: for a given value of Bo_g, θ has little or no effect. Increasing values of adhesion, on the other hand, lead to significantly larger values of σ (note that the concomitant increase of θ is just reflecting the flow phase diagram shown in Fig. 3). We hence conclude that in cohesive flows, a larger contact adhesion involves a larger plug surface roughness, as is observed for transient flows [16].

The noncohesive case, showing a clear increase of σ with θ, coincides with a flow where surface grain motion and surface deformation are possible. Many nontrivial phenomena can occur in this context, so we cannot offer any explanation for the observation reported here at this stage [41].

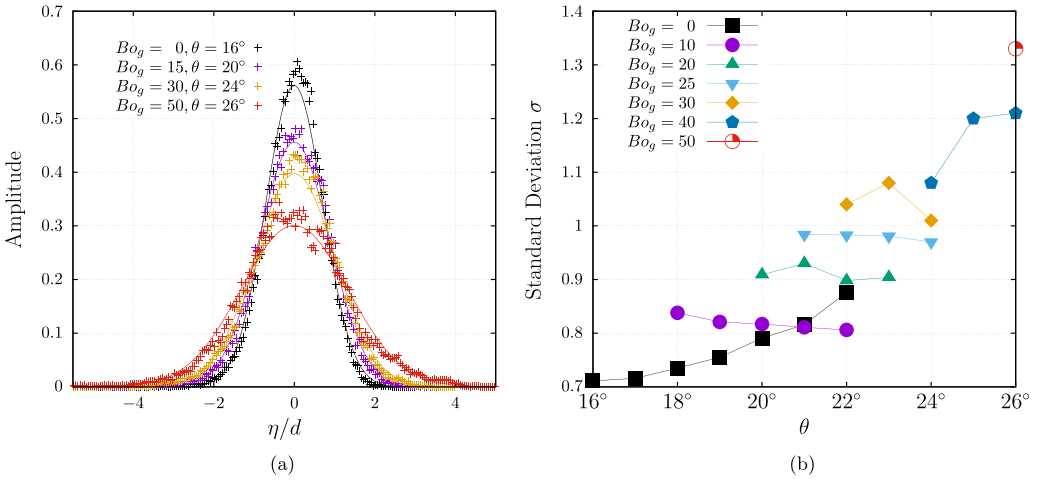

FIG. 6. (a) Probability density function of surface fluctuation η. A Gaussian distribution function $f(x) = \frac{1}{\sigma\sqrt{2\pi}} \exp(-\frac{(\eta-\bar{\eta})^2}{2\sigma^2})$ is used to fit the measurements, where $\bar{\eta}$ is the mean value of η and σ is the standard deviation of η. (b) Standard deviation of σ as a function of Bo_g and θ.

To get insight on the longitudinal details of the surface roughness, we define the two-point correlation function [33,42,43],

$$K(r) = \frac{\sum_t \left[\sum_{i=1}^{N_s-1} \sum_{j=i+1}^{N_s} \eta(x_i,t)\eta(x_j,t)\Pi(r-r_{ij})\right]}{\sum_t \left[\sum_{i=1}^{N_s-1} \sum_{j=i+1}^{N_s} \Pi(r-r_{ij})\right]}, \tag{16}$$

where $\Pi(x)$ is a step function taking the value 1 when $|x/d| < 0.5$, N_s is the number of grains located on the surface, r_{ij} is the distance between grains i and j, and t is the time.

Figure 7(a) shows the shape of $K(r)$ for noncohesive flows, for different values of the slope angle θ. We observe a significant variation of the rate of decrease with θ. To quantify this effect, we

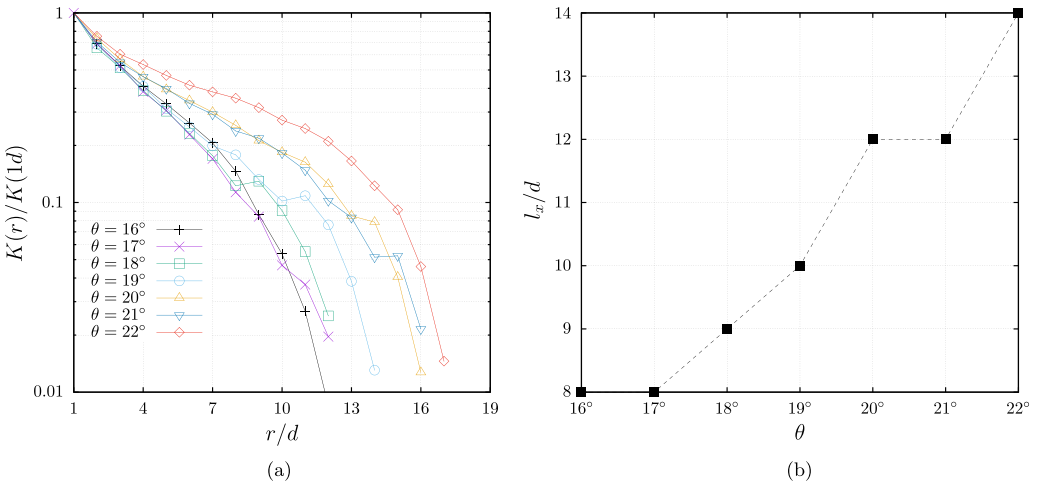

FIG. 7. (a) Pair correlation function of noncohesive flow surface fluctuation with various tilt angles θ, normalized by the value $K(r = 1d)$; x value is expressed in grain diameter. (b) A characteristic correlation length l_x is taken such that $K(l_x)/K(1d) = 0.1$ and is plotted as a function of θ.

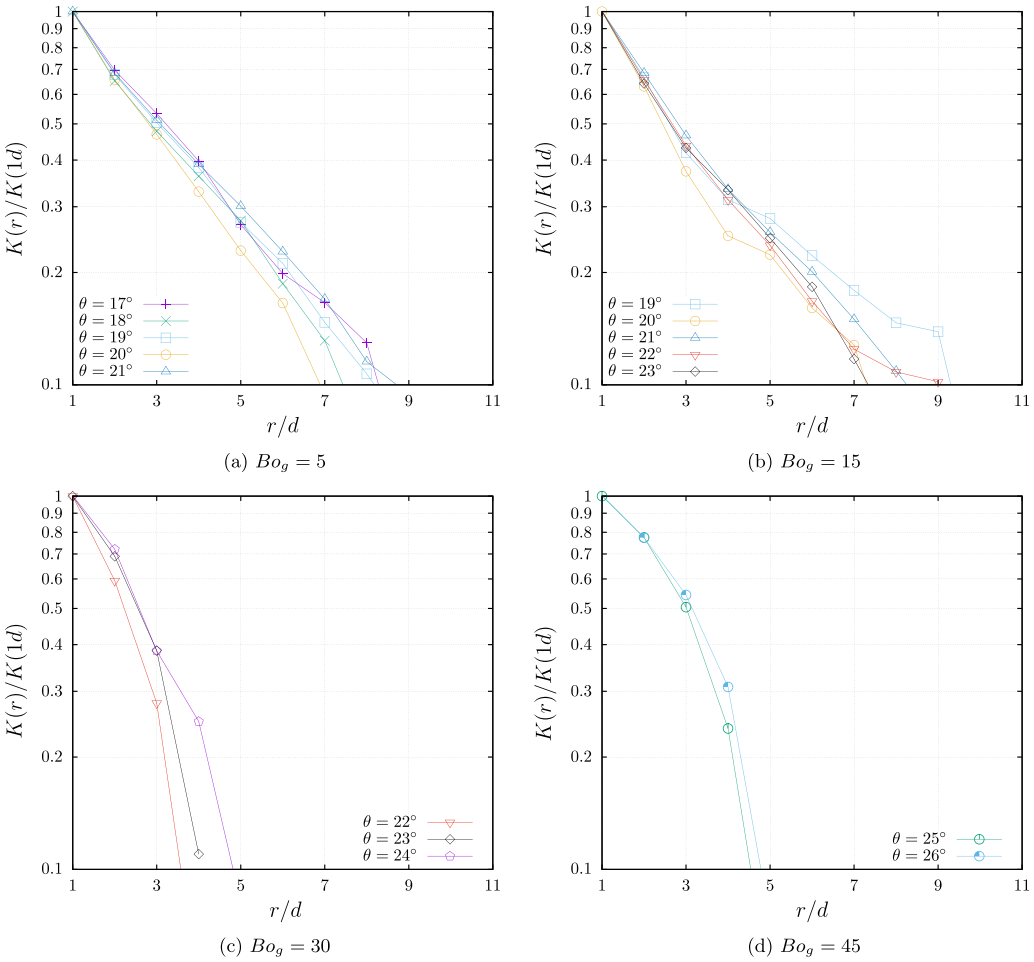

FIG. 8. Pair correlation function of cohesive flow surface fluctuation with various tilt angles θ, normalized by the value $K(r = 1d)$; x value is expressed in grain diameter: (a) $\mathrm{Bo}_g = 5$, (b) $\mathrm{Bo}_g = 15$, (c) $\mathrm{Bo}_g = 30$, and (d) $\mathrm{Bo}_g = 45$.

define the characteristic correlation length l_x as the value of r for which $K(r)/K(1d) = 0.1$ [42]. The evolution of l_x with the slope angle θ is shown in Fig. 7(b), and shows that steeper slopes induce position correlation at a longer distance. In other words, nonadhesive grains rapidly flowing tend to produce a relief with a larger wavelength than for slower flows.

The introduction of adhesive forces at contact significantly changes the overall picture. Figure 8 shows the correlation function computed for cohesive flows with varying adhesion Bo_g. We first notice that our results are consistent with those of Deboeuf and Fall, who estimated the grain aggregate size in the interval $d_{\mathrm{agg}}/d \in [4, 9]$ from matching theoretical and experimental mass flow rates [12]. Using the same definition of the correlation length l_x as for noncohesive flows, we observe that the latter decreases when Bo_g increases. This means that although the probability density function of the fluctuations of the free surface shows larger fluctuation for increasing adhesion Bo_g, the correlation length l_x tends to decrease with Bo_g. This would correspond to a more rugged profile, showing a sharper pattern.

The overall picture given by the analysis of surface fluctuations η is that the increase of contact adhesion induces significantly larger fluctuations, but that the longitudinal (following the flow

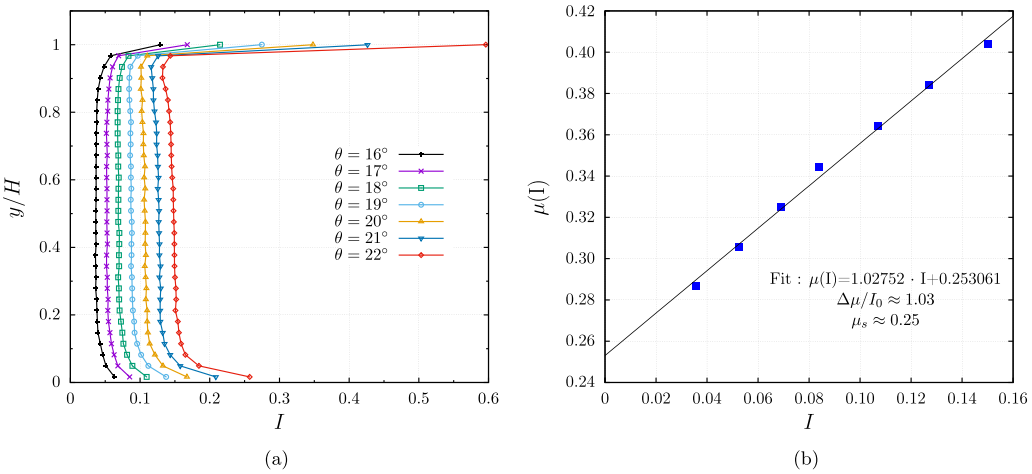

FIG. 9. (a) Inertial number profiles in discrete simulations for different slope angles θ. (b) Corresponding values of $\mu(I)$ [taken equal to $\tan(\theta)$] versus the inertial number I.

direction) characteristic length tends to be shortened, i.e., the surface profile becomes more sharply rugged. Equivalently, smaller cohesion leads to smaller surface fluctuations and a flattened smoother profile with wider relief in the longitudinal direction.

V. RHEOLOGY

A. Calibration of the $\mu(I)$ rheology

In Sec. III, a linear friction law $\mu(I)$ was introduced, supposing the independence of frictional properties on cohesive ones. Accordingly, we use noncohesive flows to calibrate the $\mu(I)$ friction law.

For noncohesive flows, Eq. (2) together with the assumption of a Bagnold scaling implies a constant I profile across the flow [7]. Consistently, Fig. 9(a) shows nearly constant profiles of I for noncohesive flow simulations ($\mathrm{Bo}_g = 0$) for θ varying between 16° and 22°, in agreement with the prediction. Free surface and bottom only show a brisk variation over two grain layers. Hence, we choose a characteristic value of I for each flow, taking the value at position $y/H = 0.5$ as a reference, thus avoiding boundary effects. Meanwhile, the friction coefficient $\mu = \mu(I)$ is readily derived from the plane inclination θ: $\mu(I) = \tan\theta$.

Figure 9(b) displays the corresponding points, nicely fitted by the affine function $\mu(I) = 1.027I + 0.253$, and thus supporting the modeling choice of a linear approximation for the $\mu(I)$ rheology [Eq. (5)]. The obtention of the values of μ_0 and $\Delta\mu/I_0$ is straightforward: the slope gives $\Delta\mu/I_0 \approx 1.03$ and the ordinate intercept gives $\mu_0 \approx 0.25$.

Now that the $\mu(I)$ relation is calibrated, we can check the analytical solution for noncohesive velocity profiles developed is Sec. V, namely, Eq. (10), with $\tau_c = 0$, i.e., $K_2 = 0$, by confronting it with data extracted from discrete simulations with no adhesion at contact, namely, with $\mathrm{Bo}_g = 0$. Therefore, for the sake of simplicity, we assume a constant volume fraction profile $\phi(z) = \phi = 0.82$, ignoring the marginal effect of bottom and surface boundary limits. We also neglect the influence of the slope θ on the value of ϕ, as suggested by Fig. 10(a). Since the $\mu(I)$ dependence was calibrated by taking values of I at $y/H = 0.5$, the comparison between analytical solution and discrete simulation is made by focusing on the agreement between data and prediction at $y/H = 0.5$. As shown in Fig. 10(b), a good collapse is obtained in the bulk. Expectedly, a slight discrepancy appears at flow bottom and surface, where point values were neglected in the friction calibration. We conclude that the calibration of μ_0 and $\Delta\mu/I_0$ is correct. Recalling the assumption that Coulombic

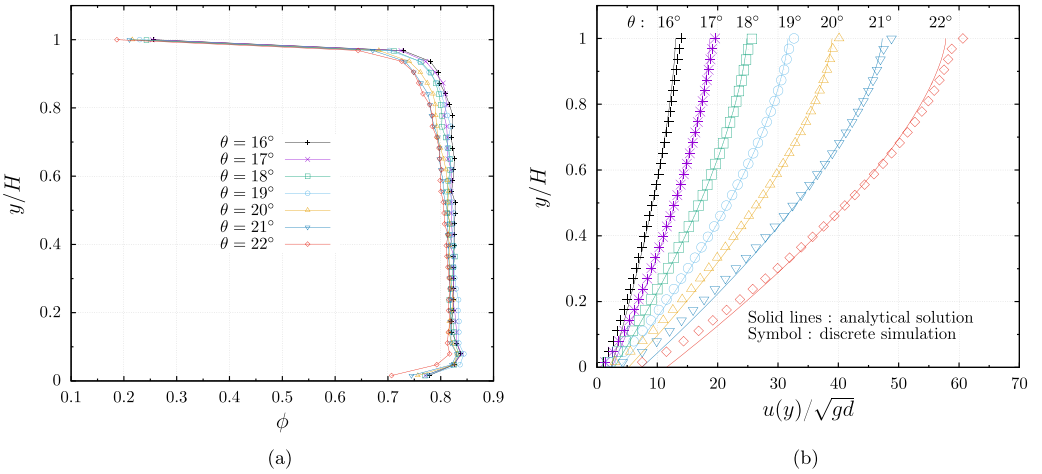

FIG. 10. For discrete simulations of noncohesive flows at different slope angles θ: (a) profiles of the volume fraction ϕ and (b) velocity profiles with the analytical solution using the rheological parameters calibrated from Fig. 9(b).

friction is not affected by the cohesive properties, the calibration achieved for $\mathrm{Bo}_g = 0$ can now be used to confront the analytical solution for cohesive velocity profiles.

B. Comparing predictions and discrete data for cohesive velocity profiles: $u_{\max}$

Now that the $\mu(I)$ dependence is adequately calibrated, we can test the analytical solution for cohesive velocity profiles, given in Eq. (10), with the outcome of discrete simulations. The agreement between analytical solutions and simulation data can either focus on the ability to reproduce the height of the plug flow, H_c, or the ability to reproduce the maximum flow velocity $u_{\max}$. The latter option is adopted in the following.

In discrete simulations, the top surface layer consists of sparse grains occasionally jumping, and is not representative of the bulk flow. For this reason, $u_{\max}$ is estimated for each discrete simulation in the second-to-last layer before the top surface. The bottom slip velocity u_{slip} is directly extracted from numerical simulations (see Sec. V E for more details and results on this aspect).

To compute the analytical solution, we suppose the volume fraction to be poorly affected by the existence of contact adhesion, so we keep $\phi = 0.82$ unchanged for all flows. The parameters μ_0 and $\Delta\mu/I_0$ are known, as is the height of the flow, H. Eventually, the only variable to be adjusted when comparing analytical and discrete flow profiles is the macroscopic cohesive stress τ_c. The value of τ_c is chosen to maximize the agreement of the surface velocity $u_{\max}$ between analytical and discrete approaches. The latter reflects the value of the local contact adhesion Bo_g, so comparing simulations with analytical solutions will provide a systematic relation between macroscopic cohesion and local microscopic adhesion. The underlying assumption of this reasoning, as stated in Sec. III, is that the cohesive stress τ_c is independent of the flow dynamics, namely, independent of the inertial number I.

The comparison of analytical and discrete cohesive velocity profiles is shown in Fig. 11, for different values of contact adhesion $\mathrm{Bo}_g = 5$, 15, 30, and 45. Considering that τ_c is the only adjusted quantity in the computation of the analytical solution, the agreement is rather good, specifically for larger contact adhesion ($\mathrm{Bo}_g = 30$ and 45). Expectedly, since the agreement was tuned on the surface velocity $u_{\max}$, the upper part of the flow is better described than the deeper parts.

The resulting relation between τ_c and Bo_g is shown in Fig. 12 (red symbols), and reads $\tau_c \approx 0.08F_c/d$, i.e., $\tau_c \approx 0.08\frac{mg}{d}\mathrm{Bo}_g$, with m the mean grain weight. The slight dispersion shown in τ_c

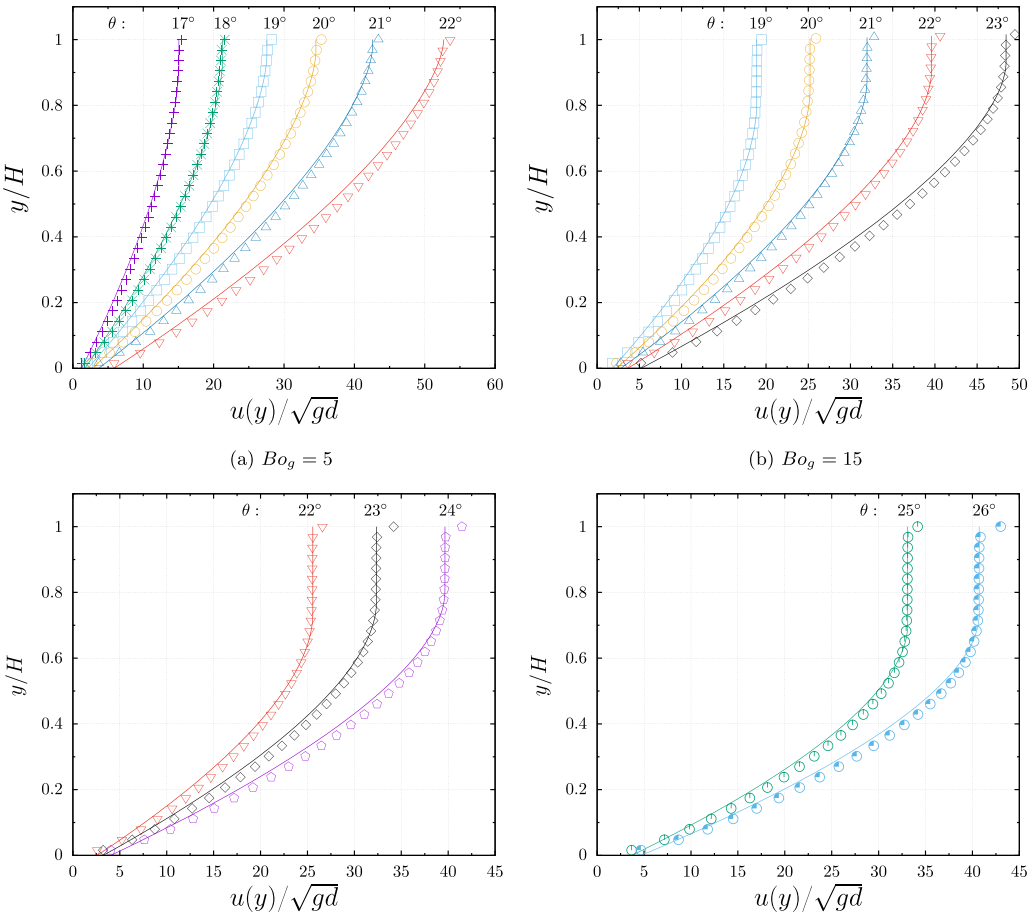

FIG. 11. Prediction $u(y)/\sqrt{(gd)}$ (solid lines) for the discrete velocity profiles $V(y)/\sqrt{gd}$ (solid symbols) at different plane inclinations θ for different contact adhesion Bo_g.

for each Bo_g corresponds to different slope angles θ, and shows how the cohesive shear stress τ_c only poorly depends on the tilt angle, thus supporting the assumption that τ_c is independent of the inertial number I.

C. Comparing predictions and discrete data for plug height H_c

Another way of investigating the dependence of cohesive stress τ_c on contact adhesion strength Bo_g is to focus on the agreement between prediction and data in terms of the plug thickness H_c, rather than in terms of the maximum velocity $u_{\max}$. The value of τ_c thus maximizing the agreement between prediction [Eq. (9)] and discrete simulation outcome is obtained for each value of contact adhesion, thus giving a new relation between cohesive yield stress τ_c and Bond number Bo_g, shown in Fig. 12. The dependence reads $\tau_c \approx 0.12 F_c/d$, i.e., $\tau_c \approx 0.12 \frac{mg}{d} \mathrm{Bo}_g$. We observe in Fig. 12 that for each value of Bo_g, the dispersion induced by the different slope angles θ is very small, mostly hidden in the symbol size.

Now that a relation between τ_c and Bo_g was yielded by comparing prediction and discrete simulations, we can rewrite Eq. (9) by replacing τ_c with its expression of Bo_g. Doing so, for each

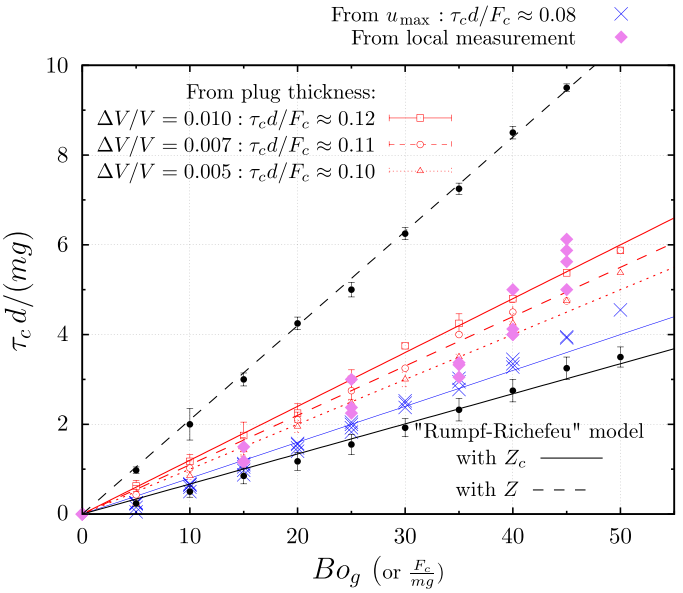

FIG. 12. Macroscopic cohesive stress τ_c (normalized by mean grain weight) as a function of contact adhesive strength Bo_g, according to different measures and predictions: matching prediction and CD simulations focusing on $u_{\max}$ (blue cross), or focusing on H_c including different $\Delta V/V$ cutoff values (red symbols), and local measurements presented in Sec. V C (purple diamonds). Black dots show the Rumpf-Richefeu prediction [Eq. (19)] considering the average number of contacts per particle, Z (dashed line), and the average number of cohesive contacts per particle, Z_c (solid line).

value of Bo_g, Eq. (9) becomes a function of the slope angle:

$$\frac{H_c}{H} = \frac{1}{(\tan\theta - \mu_0)\phi\cos\theta}\frac{\tau_c}{\rho g H},$$
$$H_c = 0.12\frac{m}{\rho\phi d}\frac{\mathrm{Bo}_g}{(\tan\theta - \mu_0)\cos\theta}, \tag{17}$$

where all quantities are constant but the slope angle, varying for each Bo_g according to the flow phase diagram shown in Fig. 3.

The outcome of the prediction is shown in Fig. 13. Given the absence of any adjusting parameter, the agreement between data and predictions is rather correct. We observe, nevertheless, how the agreement gets better for larger values of Bo_g but deteriorates for smaller adhesion, particularly for $\mathrm{Bo}_g = 5$, for which discrete simulations produce a poorly defined plug area.

We note that the prefactor obtained here from the analysis of H_c is larger than when τ_c is estimated from the maximum velocity. In other words, for a given value of τ_c well describing $u_{\max}$, H_c would be underestimated. Conversely, a value of τ_c well describing H_c would overestimate $u_{\max}$.

We may suppose that the value of the linear coefficient characterizing the relation between τ_c and F_c/d stemming from comparison between prediction and discrete simulation of the plug flow height H_c is likely to depend on the criteria chosen for the shear rate cutoff value, as discussed in Sec. IV A. To assert the sensitivity of the measures on the latter, we test different cutoff values $\Delta V/V = 0.007$ and $\Delta V/V = 0.005$ for the calculation of the plug thickness from discrete simulations, and compare the new sets of values for H_c with prediction [Eq. (9)]. The different relations between τ_c and F_c/d

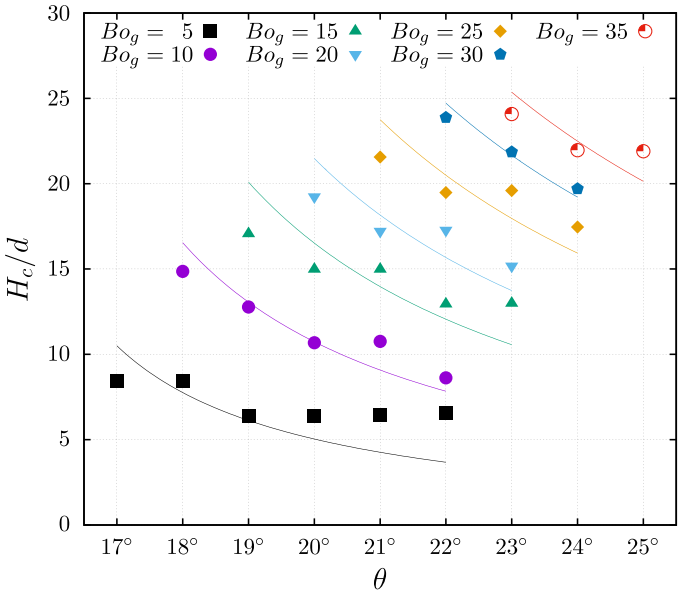

FIG. 13. Prediction of the plug thickness H_c as a function of contact adhesion Bo_g and tilt angle θ, based on Eq. (9) using $\tau_c \approx 0.12 F_c/d$ as yielded by discrete simulations. Solid symbols show the measurements extracted from discrete simulations.

are summarized in the following, and also reported in Fig. 12:

$$\begin{aligned} \tau_c &\approx 0.12 F_c/d \quad \text{with} \quad \Delta V/V = 0.01, \\ \tau_c &\approx 0.11 F_c/d \quad \text{with} \quad \Delta V/V = 0.007, \\ \tau_c &\approx 0.10 F_c/d \quad \text{with} \quad \Delta V/V = 0.005. \end{aligned} \tag{18}$$

We observe that smaller prefactors are observed for smaller cutoff values of $\Delta V/V$, involving, however, small variations between the different cases. We thus conclude that the sensitivity to the criteria applied to extract the plug flow height from discrete simulations is weak.

We notice that the relation between τ_c and Bo_g yielded by the measure of H_c differs from the relation yielded by the measure of $u_{\max}$ (Sec. V C). One reason could be that the definition of H_c in the model is a very strict one: $\dot{\gamma} = 0$ for $y \in [H - H_c, H]$, while creep motion is in reality present at $y \approx H - H_c$. As a result, H_c as measured in discrete flows is larger than the definition of H_c in the model, which results in a larger prefactor to adjust to the value of τ_c. On the other hand, the measure of $u_{\max}$ from the velocity profiles displayed by the simulations is precise. The discrepancy between the two relations, given by measuring either $u_{\max}$ or H_c, remains, however, reasonable, although it does point out a disagreement between the model and the behavior of discrete simulations.

D. Addressing Rumpf's prediction

The relation between the macroscopic cohesive stress and the local contact adhesive strength was questioned in Rumpf's seminal work [18], and later reworked by Richefeu *et al.* [19], both aiming to derive the macroscopic properties from contact-scale interactions including the structure of the packing and its frictional properties. Adapting their ideas to 2D systems yields the following prediction for the cohesive stress τ_c [21]:

$$\frac{\tau_c}{\rho g} = \frac{d}{4} \mu_s \phi Z \mathrm{Bo}_g, \tag{19}$$

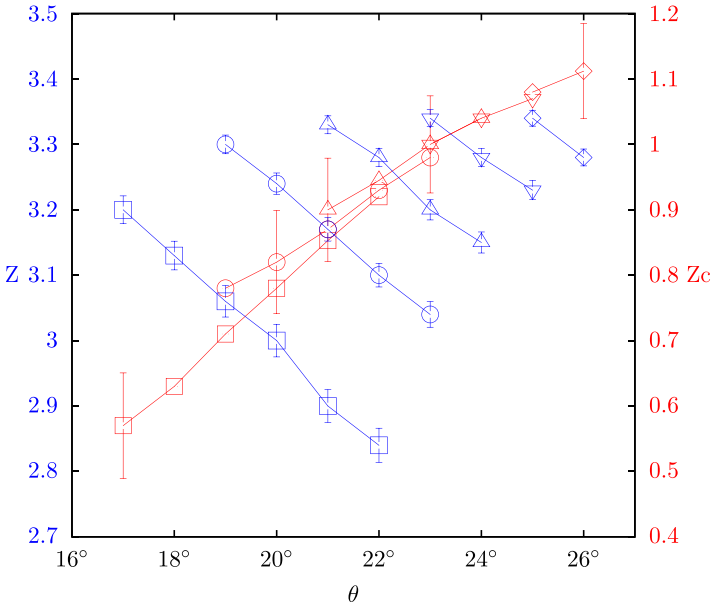

FIG. 14. Coordination number Z (open blue symbols) and adhesive coordination number Z_c (open red symbols), as a function of the slope angle θ, for different adhesive strength Bo_g: □, 5; ◯, 15; △, 25; ▽, 35; and ◇, 45. The error bars show the standard deviation characterizing the time fluctuations.

where μ_s is the internal friction coefficient, Z is the average number of contacts per particle (or coordinance), ϕ is the volume fraction, and Bo_g characterizes the contact adhesion strength.

To investigate the accuracy of this prediction for the case of the cohesive flows simulated here, we set $\mu_s = \mu_0 = 0.25$ obtained from the calibration on the $\mu(I)$ rheology in Sec. V A. In addition, we take a constant volume fraction $\phi \approx 0.82$ as measured. This is of course a simplification, since the volume fraction is affected by the existence and the intensity of adhesion force. The latter effect also shows in the mean number of contacts per grain, Z. This quantity being more meaningful in the sense that contacts directly contribute to the mechanical properties of the packing, we chose to focus on the sensitivity of Z to adhesion, while keeping ϕ a constant for the sake of simplicity.

The value of Z is extracted from the simulations: $Z = 2N_{\mathrm{contact}}/N_p$, where N_{contact} refers to the time-averaged contact number for each flow and N_p to the total number of grains. Figure 14 shows the behavior of Z with the tilt angle θ for different values of the adhesive strength Bo_g. We observe how increasing adhesion Bo_g leads to a larger coordinance Z. For a given value of Bo_g, however, increasing the tilt angle θ leads to looser packings with smaller Z. These values injected in Eq. (19) yield $\tau_c \approx 0.21 F_c/d$, reported in Fig. 12, which is obviously a larger estimation than those based on comparing predictions and simulations for $u_{\max}$ and H_c.

Instead of considering the mean number of contacts per particle, Z, Abramian *et al.* [21] used the mean number of cohesive contacts per particle, Z_c, and thereby obtained a good agreement between 2D numerical simulations and the "Rumpf-Richefeu" prediction [Eq. (19)]. Following this idea, we measure Z_c as a function of θ for all values of Bo_g, as shown in Fig. 14. The mean adhesive coordination number Z_c is found to increase with θ consistently for all values of Bo_g. Injecting these values in Eq. (19) yields $\tau_c \approx 0.067 F_c/d$. We note that this result is in much better agreement with the results yielded by comparison between prediction and simulation focusing on $u_{\max}$ ($\tau_c \approx 0.08 F_c/d$). This prediction is also in good agreement with the linear fit extracted from numerical data by Mandal *et al.* [20], who obtained $\tau_c \approx 0.07 F_c/d^2$ in three dimensions.

It is worth noting that the relation in Eq. (19) being very sensitive to the details of the microstructure, with ϕ, Z, and μ all equally weighty in the prediction, arguing for or against the latter remains

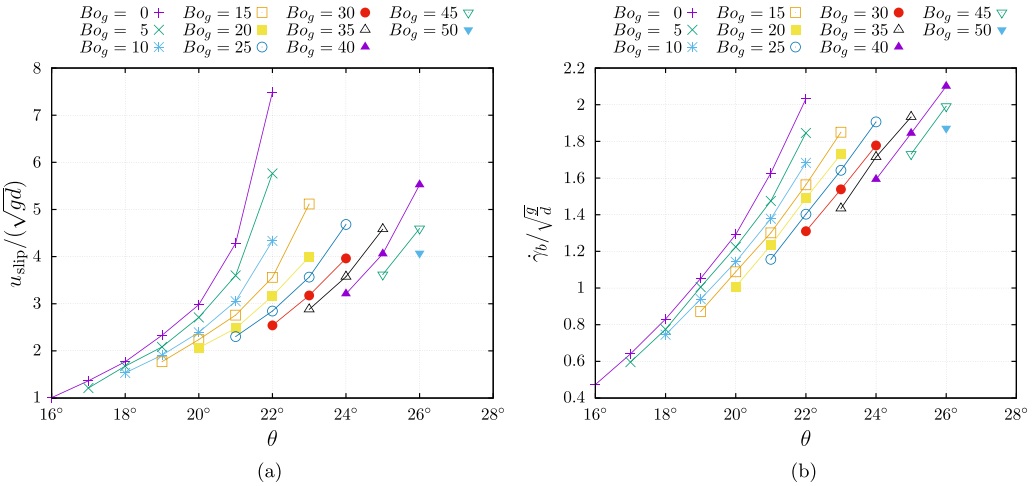

FIG. 15. (a) Normalized slip velocity $u_{\text{slip}}/\sqrt{gd}$ and (b) normalized bottom shear rate $\dot{\gamma}_b/\sqrt{g/d}$, as a function of θ for all values of Bo_g explored.

difficult. However, the linearity of the dependence between macroscopic τ_c and contact-scale Bo_g is clearly supported by the numerical data.

E. Wall slip

We extract u_{slip} from discrete numerical simulations by averaging the grains' horizontal velocity in the bottom layer ($y/d \leqslant 1$) over the steady flow duration. Figure 15(a) displays u_{slip} as a function of the tilt angle θ for all values of the adhesive strength Bo_g. We observe how u_{slip} increases with θ, but consistently decreases with Bo_g: a steeper inclined plane favors slipping at the bottom, and stronger adhesion between particles and bottom attenuates slipping motion (we recall that contact properties are the same whether they involve flowing grains only or flowing grains and bottom roughness grains).

Next, we compute the flow shear rate near the bottom, $\dot{\gamma}_b$, by considering the difference in the two bottom layers' velocities, divided by the vertical distance between them. Figure 15(b) shows $\dot{\gamma}_b$ as a function of θ for all values of the adhesive strength Bo_g. We observe that $\dot{\gamma}_b$ increases linearly with θ, and that Bo_g has a marginal influence on the increasing rate.

In order to test the Navier-Robin boundary condition, we plot u_{slip} versus $\dot{\gamma}_b$. As shown in Fig. 16, the data support the Navier-Robin condition as long as $\dot{\gamma}_b/\sqrt{g/d} \lesssim 1.6$, with $\lambda_{\text{slip}} = u_{\text{slip}}/\dot{\gamma}_b \approx 2d$ regardless of Bo_g. The slipping length λ_{slip} thus appears to be independent of the adhesive contact strength Bo_g in the flow regimes where it can be unambigously defined.

Hence, we conclude that the behavior observed at boundaries for dry flows [22,23] holds in the case of cohesive flows for moderate velocities, and that the slipping length is poorly influenced by adhesive properties.

VI. DISCUSSION

In this contribution, simple discrete simulations of cohesive chute flows were performed to assess the reliability of a continuum model based on a number of assumptions, namely, (i) an ideal Coulomb rheology $\tau = \mu P + \tau_c$, (ii) a linear dependence of the friction coefficient μ and the inertial number I in the noncohesive case, and (iii) the independence of cohesion τ_c on friction

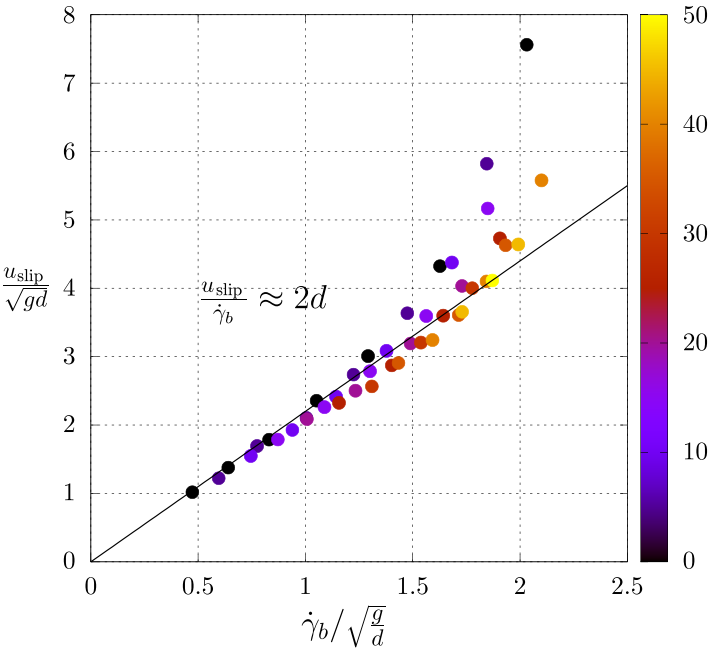

FIG. 16. Normalized slipping velocity $u_{\text{slip}}/\sqrt{gd}$ as a function of normalized bottom shear rate $\dot{\gamma}|_b/\sqrt{g/d}$. The color bar gives the value of Bo_g.

μ and inertial number I, and of friction μ on cohesion τ_c. The relatively good performances of the model to describe the discrete simulation velocity profiles (as shown in Fig. 11) are an indirect indication that these hypotheses are sensible, even though extremely simple and based on a classical inertial number without cohesive addition as in Ref. [14].

Besides this indirect verification, discrete simulations also provide a direct insight into the behavior of the flows. For instance, the linearity of the $\mu(I)$ dependence was first verified in Sec. V A through direct measurement of the inertial number I in the case of noncohesive flows [verifying hypothesis (ii)]. In the same way, flow laws obeyed by cohesive flows can be probed at any depth y, relating the local shear rate $\tau(y) = \phi\rho g(H - y)\sin\theta$ to the local pressure $P(y) = \phi\rho g(H - y)\cos\theta$. Using the fact that the inertial number I is no longer a constant in cohesive flows [Fig. 17(a)] [10,20], we can single out a given value of I, considering different depth y in different flows (i.e., for different θ) while keeping Bo_g constant, as is illustrated in Fig. 17(a). This allows us to plot local values $\tau(y)$ as a function of $P(y)$ for each value of I at the given depth y and for a given cohesion, uncovering the validity of the ideal Coulomb material assumption. The plots, as displayed in Fig. 17(b), actually reveal neat affine functions, which allows us to validate the use of the Coulomb rheology $\tau = \mu P + \tau_c$ [verifying hypothesis (i)]. The slope giving the coefficient of friction μ and the locus the cohesive stress τ_c, we have access to these quantities for all values of Bo_g, hence all pairs (θ, Bo_g) shown in Fig. 3, and for various values of I. We can thus plot μ as a function of I for all the values of Bo_g considered; the result is shown in Fig. 18(a). A first remark is that the trend is the same for most values of the adhesion Bo_g, corroborating the independence of friction on cohesive properties [verifying hypothesis (iii)]. We should note, however, that for large adhesion, $\text{Bo}_g = 45$, the dependence significantly differs; yet it is difficult to conclude on this deviation from the main trend, the flow getting very thin for this large adhesion due to an expanding plug, and finite-size effects becoming possible. We also notice that the results match and support the $\mu(I)$ dependence established for noncohesive flows in Sec. V A [hypothesis (ii)].

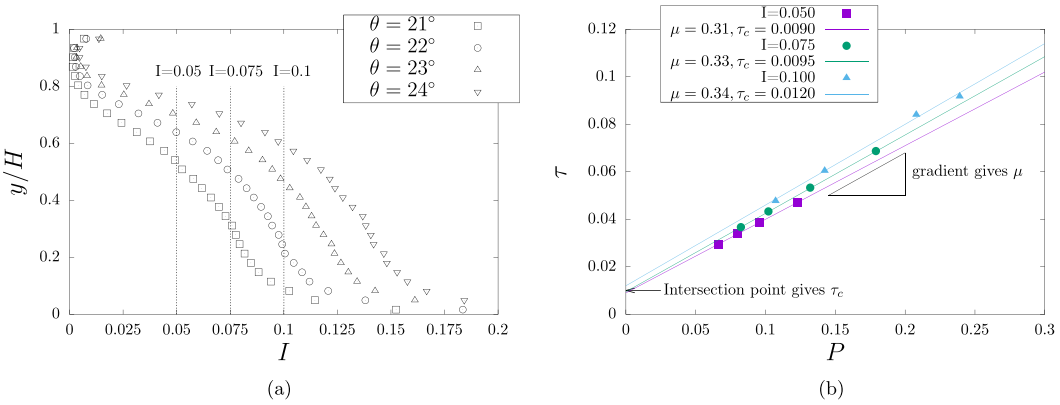

FIG. 17. (a) Inertial number profile $I(y)$ for stationary uniform flows for $\mathrm{Bo}_g = 25$ and different tilt angle θ: identical values of I are reached at different y for different slopes θ. (b) Corresponding shear stress τ plotted versus P for (y, θ) pairs for the three illustrated values of I, approximated by an affine dependence supporting Eq. (3).

Figure 18(b) shows the behavior of τ_c with I for all the values of Bo_g considered. We observe that any dependence is hardly visible, so we conclude that the assumption that τ_c is independent of I is supported by the discrete simulation [hypothesis (iii)]. The steady increase of τ_c with the adhesion-related Bo_g is, however, clearly apparent, and reported in Fig. 12 for all simulation points. While we observe a general agreement with the values reported from comparing continuum and discrete approaches, we nevertheless notice that these new local (namely, at a given location y) data no longer unambiguously support the linearity expected in the Rumpf prediction between τ_c and Bo_g.

The discrete simulations also offer an interesting insight into the effect of contact adhesion onto the aspect of the flow surface. The overall picture given by the analysis of surface fluctuations is that the increase of contact adhesion, inducing an increase of macroscopic cohesion, leads to significantly larger fluctuations. Yet the longitudinal (following the flow direction) characteristic length tends to be shortened. In other words, the surface profile becomes sharper. Equivalently,

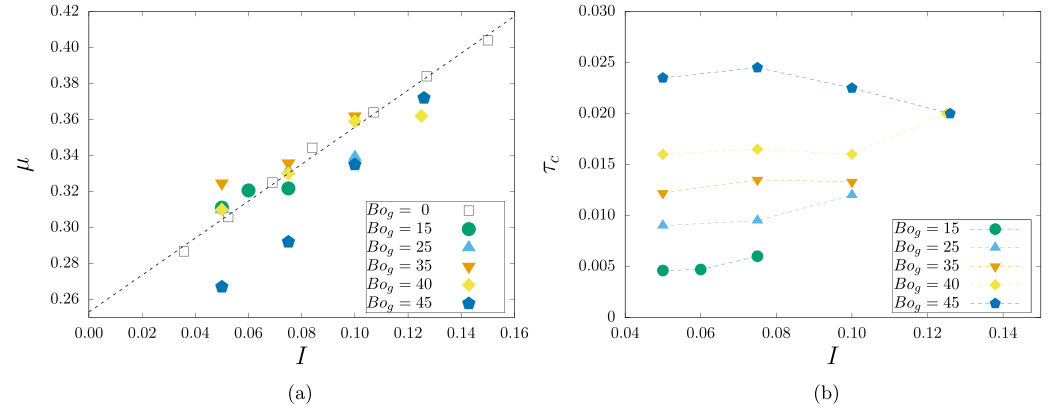

FIG. 18. (a) Local value of the friction μ versus I determined locally at different depths y for different values of Bo_g; the dotted gray line shows the friction law $\mu(I) = \mu_0 + \Delta\mu/I_0 \times I$ calibrated from noncohesive flows (Sec. V A). (b) Variations of local τ_c versus I, both determined locally at different depths y, for different values of Bo_g.

smaller cohesion leads to smaller surface fluctuations and a flattened smoother surface profile with wider relief in the longitudinal direction.

Significantly, the analysis of bottom velocities for all contact adhesion and incline slopes explored shows that a Navier-Robin boundary condition, as evidenced by Artoni *et al.* for noncohesive flows [22,23], remains valid in the case of cohesive ones at moderate velocities, with a slipping length poorly dependent on adhesion properties.

But most importantly, by combining discrete simulation and analytical analysis, this work allows for an informed analysis of the cohesive granular rheology. The discrete simulation results support the ideal Coulomb material model, whereby effective frictional properties and macroscopic cohesion are independent properties. It also makes a strong case for the relevance of linearized $\mu(I)$ dependence, at least for moderate values of I. Remarkably, the latter gives satisfactory results for a classical definition of the inertial number as first applied for dry flows [8], without the introduction of modification accounting for the existence of contact adhesion [13,14]. In other words, many specific features of cohesive flows are captured by relatively basic ingredients, namely, a local $\mu(I)$ rheology for dry flows augmented with a constant cohesive stress.

In terms of scale transition, the results are globally in favor of a linear relation between local contact-scale adhesion and macroscopic system-scale cohesion, as first proposed by Rumpf [18].

Because the work is based on relatively accessible quantities in laboratory measurements, it may give interesting hints in the framework of experimental work. In particular, the role of the bottom velocity can be questioned, or the appearance of a flow surface pattern partially interpreted. At any rate, in the context of a simplified configuration, the work contributes to clarifying the intricate roles of contact adhesion and flow dynamics in the behavior of cohesive granular flows.

DATA AVAILABILITY

There are no publicly available research data or software supporting this manuscript. Requests for further information or data should be sent to the authors.

APPENDIX: INFLUENCE OF THE RESTITUTION COEFFICIENT ON COHESIVE PROPERTIES

The influence of the value of the coefficient of restitution at contact e on the kinematics of the flow, as well as on its cohesive properties, is assessed by varying it value between 0 and 0.80, setting it successively to 0.05, 0.10, 0.20, and 0.50 in this interval.

Therefore, we consider a flow of length $L \approx 80d$ and height $H \approx 54d$, with grain diameter uniformly distributed in the interval $[d_{\min}, d_{\max}]$, $d_{\max}/d_{\min} = 1.5$ ($\langle d \rangle = 0.005$). The adhesion is fixed by setting Bo_g to 30, and the slope is $\theta = 24.5^\circ$.

A first simple indication is given by the evolution of the mean flow velocity with time, shown in Fig. 19(a). We observe that up to $e = 0.20$, the mean behavior of the flow is essentially unchanged. This shows how a zero restitution and weak values of restitution are, if maybe not strictly equivalent, leading nevertheless to a very similar behavior. On the contrary, the effect of restitution is very clear for $e = 0.5$, for which the mean velocity takes larger values, and the stationary regime is not reached over the flow duration considered. It becomes more dramatic for $e = 0.8$, for which the mean velocity is considerably larger, and the stationary regime may actually not exist for this value of slope and adhesion. Expectedly, larger restitution meaning less energy dissipation, the flow kinetic energy increases, without, however, giving a clear insight on the cohesive properties.

The mean velocity gives an averaged picture, which does not allow to distinguish rapid flow and plug surface; hence it conceals any possible effect of e on the cohesive properties of the flow. The latter are, however, revealed by plotting the velocity profile over the last moments of the flow: $t/\sqrt{(H/g)} \in [100, 120]$, for which the stationary regime is attained for $e \in [0, 0.20]$, but not for $e = 0.5$ or $e = 0.8$. The outcome is plotted in Fig. 19(b). We observe a slight increase of velocity for $e = 0.20$ compared to the case $e = 0$; this increase remains, however, very small for $e < 0.20$. For these small values of restitution, no measurable effect on the plug height H_c is visible. Interestingly,

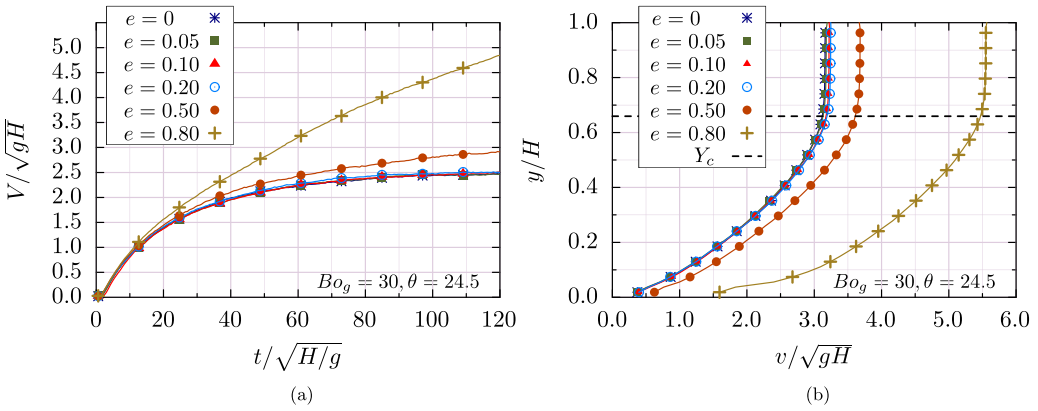

FIG. 19. (a) Normalized mean velocity $V/\sqrt{gH}$ as a function of the nomalized time $t/\sqrt{H/g}$, and (b) normalized velocity profile $v/\sqrt{gH}$ computed over the time interval $t/\sqrt{(H/g)} \in [100, 120]$, for a contact adhesion $\mathrm{Bo}_g = 30$ and a slope $\theta = 24.5^\circ$, for different values of the contact restitution coefficient $e \in [0 : 0/80]$.

no obvious effect is visible either for larger values $e = 0.5$ and $e = 0.8$, even though the kinematics is significantly more developed. It is tempting to conclude that the restitution coefficient has no effect on cohesion; however, since the stationary regime was not attained for $e = 0.5$ and $e = 0.8$, we cannot conclude on the basis of the corresponding profiles shown in Fig. 19(b). However, prediction (9) for H_c being independent of the frictional properties of the flow, $\Delta\mu$, but only dependent on the static friction μ_0 (unlike $u_{\max}$, for instance), this result is not entirely surprising. In the framework of 2D simulations of cohesive flows on inclines as presented here, we can, however, safely conclude that e has a very weak effect on cohesion for $e \leqslant 0.20$, and that the choice $e = 0$ for the simulations analyzed in this paper is a simple yet reasonable choice for studying the basics of cohesive flows.

We can apply for these flows the prediction in Eq. (9) for H_c, using the relation between cohesive stress and adhesion yielded by the analysis of plug height performed in Sec. V C, and reported in Fig. 12: $\tau_c = 0.012\frac{mg}{d}\mathrm{Bo}_g$. We obtain $H_c/d = 18.4$. The corresponding predicted height Y_c of the bottom of the surface plug slab is reported in Fig. 19(b), and shows a fair concordance with the velocity profiles exhibited by the discrete simulations.

[1] B. Andreotti, Y. Forterre, and O. Pouliquen, *Granular Media: Between Fluid and Solid* (Cambridge University Press, Cambridge, UK, 2013).

[2] J.-P. Gras, J.-Y. Delenne, and M. Youssoufi, Study of capillary interaction between two grains: A new experimental device with suction control, Granular Matter **15**, 49 (2013).

[3] K. R. LaMarche, F. J. Muzzio, T. Shinbrot, and B. J. Glasser, Granular flow and dielectrophoresis: The effect of electrostatic forces on adhesion and flow of dielectric granular materials, Powder Technol. **199**, 180 (2010).

[4] Y. Wu, Y. Sun, and D. Wang, The combined effect of cohesion and finite size on the collapse of wet granular columns, Soft Matter **19**, 9520 (2023).

[5] R. S. Sharma, W. Sarlin, L. Xing, C. Morize, P. Gondret, and A. Sauret, Effects of interparticle cohesion on the collapse of granular columns, Phys. Rev. Fluids **9**, 074301 (2024).

[6] A. Pol, R. Artoni, and P. Richard, Cohesive granular material in a rotating drum: Flow regimes and size effects, J. Fluid Mech. **1006**, A24 (2025).

[7] L. E. Silbert, D. Ertaş, G. S. Grest, T. C. Halsey, D. Levine, and S. J. Plimpton, Granular flow down an inclined plane: Bagnold scaling and rheology, Phys. Rev. E **64**, 051302 (2001).
[8] GDR MiDi, On dense granular flows, Eur. Phys. J. E **14**, 341 (2004).
[9] R. Brewster, G. S. Grest, J. W. Landry, and A. J. Levine, Plug flow and the breakdown of Bagnold scaling in cohesive granular flows, Phys. Rev. E **72**, 061301 (2005).
[10] P. G. Rognon, J.-N. Roux, M. Naaim, and F. Chevoir, Dense flows of cohesive granular materials, J. Fluid Mech. **596**, 21 (2008).
[11] N. Preud'homme, G. Lumay, N. Vandewalle, and E. Opsomer, Numerical measurement of flow fluctuations to quantify cohesion in granular materials, Phys. Rev. E **104**, 064901 (2021).
[12] S. Deboeuf and A. Fall, Cohesion and aggregates in unsaturated wet granular flows down a rough incline, J. Rheol. **67**, 909 (2023).
[13] T.-T. Vo, S. Nezamabadi, P. Mutabaruka, J.-Y. Delenne, and F. Radjai, Additive rheology of complex granular flows, Nat. Commun. **11**, 1476 (2020).
[14] L. Braysh, P. Mutabaruka, F. Radjai, and S. Mora, Dynamics of wet granular flows down an inclined plane, J. Rheol. **69**, 409 (2025).
[15] H. Alarcón, J.-C. Géminard, and F. Melo, Effect of cohesion and shear modulus on the stability of a stretched granular layer, Phys. Rev. E **86**, 061303 (2012).
[16] A. Abramian, P.-Y. Lagrée, and L. Staron, How cohesion controls the roughness of a granular deposit, Soft Matter **17**, 10723 (2021).
[17] F. Tapia, S. Santucci, and J.-C. Géminard, Fracture reveals clustering in cohesive granular matter, Europhys. Lett. **115**, 64001 (2016).
[18] H. Rumpf, Zur theorie der zugfestigkeit von agglomeraten bei kraftübertragung an kontaktpunkten, Chem. Ing. Tech. **42**, 538 (1970).
[19] V. Richefeu, M. S. El Youssoufi, and F. Radjaï, Shear strength properties of wet granular materials, Phys. Rev. E **73**, 051304 (2006).
[20] S. Mandal, M. Nicolas, and O. Pouliquen, Insights into the rheology of cohesive granular media, Proc. Natl. Acad. Sci. USA **117**, 8366 (2020).
[21] A. Abramian, L. Staron, and P.-Y. Lagrée, The slumping of a cohesive granular column: Continuum and discrete modeling, J. Rheol. **64**, 1227 (2020).
[22] R. Artoni and A. C. Santomaso, Effective wall slip in chutes and channels: Experiments and discrete element simulations, Granular Matter **16**, 377 (2014).
[23] R. Artoni, A. C. Santomaso, M. Go', and P. Canu, Scaling laws for the slip velocity in dense granular flows, Phys. Rev. Lett. **108**, 238002 (2012).
[24] T. Wang, L. Jing, C. Kwok, Y. D. Sobral, T. Weinhart, and A. R. Thornton, Basal layer of granular flow down smooth and rough inclines: Kinematics, slip laws and rheology, J. Fluid Mech. **1025**, A27 (2025).
[25] O. Pouliquen, Powders and cohesive granular media: a rheological perspective, Rheol Acta **64**, 195 (2025).
[26] P. A. Cundall and O. D. L. Strack, A discrete numerical model for granular assemblies, Géotechnique **29**, 47 (1979).
[27] J. J. Moreau, Some numerical methods in multibody dynamics: application to granular material, Eur. J. Mech. A Solids **13**, 93 (1994).
[28] F. Radjai and V. Richefeu, Contact dynamics as a nonsmooth discrete element method, Mech. Mater. **41**, 715 (2009).
[29] L. Staron, L. Duchemin, and P.-Y. Lagrée, Cohesive granular columns collapsing: Numerics questioning failure, cohesion, and friction, J. Rheol. **67**, 1061 (2023).
[30] F. Ma, P.-Y. Lagrée, and L. Staron, Exploring the gravity-driven failure of a cohesive granular column, Phys. Rev. E **111**, 055401 (2025).
[31] A. Gans, O. Pouliquen, and M. Nicolas, Cohesion-controlled granular material, Phys. Rev. E **101**, 032904 (2020).
[32] O. Pouliquen, Scaling laws in granular flows down rough inclined planes, Phys. Fluids **11**, 542 (1999).
[33] L. Staron, Correlated motion in the bulk of dense granular flows, Phys. Rev. E **77**, 051304 (2008).
[34] P.-Y. Lagrée, http://basilisk.fr/sandbox/M1EMN/Exemples/bagnold_periodic_cohesif.c (2019).

[35] P. Pierrat, D. K. Agrawal, and H. S. Caram, Effect of moisture on the yield locus of granular materials: Theory of shift, Powder Technol. **99**, 220 (1998).
[36] S. Mandal and D. V. Khakhar, A study of the rheology of planar granular flow of dumbbells using discrete element method simulations, Phys. Fluids **28**, 103301 (2016).
[37] S. Patro, M. Prasad, A. Tripathi, P. Kumar, and A. Tripathi, Rheology of two-dimensional granular chute flows at high inertial numbers, Phys. Fluids **33**, 113321 (2021).
[38] P. Jop, Y. Forterre, and O. Pouliquen, A constitutive law for dense granular flows, Nature (London) **441**, 727 (2006).
[39] F. da Cruz, S. Emam, M. Prochnow, J.-N. Roux, and F. Chevoir, Rheophysics of dense granular materials: Discrete simulation of plane shear flows, Phys. Rev. E **72**, 021309 (2005).
[40] N. Berger, E. Azéma, J.-F. Douce, and F. Radjai, Scaling behaviour of cohesive granular flows, Europhys. Lett. **112**, 64004 (2015).
[41] Y. Forterre and O. Pouliquen, Long-surface-wave instability in dense granular flows, J. Fluid Mech. **486**, 21 (2003).
[42] O. Pouliquen, Velocity correlations in dense granular flows, Phys. Rev. Lett. **93**, 248001 (2004).
[43] O. Baran, D. Ertaş, T. C. Halsey, G. S. Grest, and J. B. Lechman, Velocity correlations in dense gravity-driven granular chute flow, Phys. Rev. E **74**, 051302 (2006).